Effect of Simultaneous Substitution of Y and Ta on the Stabilization of Cubic Phase, Microstructure, and Li$^+$ Conductivity of Li$_7$La$_3$Zr$_2$O$_{12}$ Lithium Garnet

L. Dhivya and Ramaswamy Murugan*

Department of Physics, Pondicherry University, Puducherry 605 014, India

S *Supporting Information*

ABSTRACT: Garnet-type lithium stuffed oxide Li$_7$La$_3$Zr$_2$O$_{12}$ (LLZ) in the cubic phase has received significant attention because of its high Li$^+$ conductivity at room temperature and excellent stability against lithium metal anodes. In addition to the high Li$^+$ conductivity, the dense microstructure is also a critical issue for the successful application of LLZ as a solid electrolyte membrane in all-solid-state lithium and lithium–air batteries. The stabilization of LLZ in the cubic phase with dopants indicated a reduction in sintering temperature with La^{3+} site doping and improved conductivity by doping the Zr^{4+} site. However, there are only a few reports regarding the simultaneous substitution on the La^{3+} and on the Zr^{4+} site in LLZ. In the present study, systematic investigations have been carried out on Li$_{7-x}$La$_{3-y}$Y$_y$Zr$_{2-x}$Ta$_x$O$_{12}$ (x = 0.4, y = 0, 0.125, 0.25, and 0.5) to understand the effect of simultaneous substitution of Y^{3+} for La^{3+} and Ta^{5+} for Zr^{4+} in LLZ on the stabilization of the high conductive cubic phase, microstructure, and Li$^+$ conduction behavior. Powder X-ray diffraction (PXRD) revealed the stabilization of a cubic-like garnet structure for the entire selected compositional range of Li$_{7-x}$La$_{3-y}$Y$_y$Zr$_{2-x}$Ta$_x$O$_{12}$ (x = 0.4, y = 0, 0.125, 0.25, and 0.5) samples sintered at 750 °C. However, the Raman spectra revealed that the cubic phase stabilized at around 750 °C for the Li$_{7-x}$La$_{3-y}$Y$_y$Zr$_{2-x}$Ta$_x$O$_{12}$ (x = 0.4, y = 0, 0.125, 0.25, and 0.5) samples is different from the high Li$^+$ conductive cubic phase ($Ia\bar{3}d$), and the transformation to the high Li$^+$ conductive cubic phase with a distorted lithium sublattice ($Ia\bar{3}d$) is observed only for the samples sintered at elevated temperature. Preliminary thermogravimetric (TG), Raman, and Fourier transform infrared (FTIR) studies indicated that the observed low temperature cubic phase of the investigated samples sintered at 750 °C might result from insertion of water vapor from the humid atmosphere into the crystal lattice and subsequent replacement of the lithium ions by protons to form O–H bonds. The AC impedance analysis indicated that the optimal Y substitution in Li$_{7-x}$La$_{3-y}$Y$_y$Zr$_{2-x}$Ta$_x$O$_{12}$ (x = 0.4, y = 0.125 and 0.25) helps to reduce the grain boundary resistance in a major way and also helps to reduce the bulk resistance slightly. Among the investigated compositions, Li$_{6.6}$La$_{2.75}$Y$_{0.25}$Zr$_{1.6}$Ta$_{0.4}$O$_{12}$ sintered at 1200 °C exhibits a maximized room temperature total (bulk + grain boundary) Li$^+$ conductivity of 4.36 × 10^{-4} S cm^{-1} along with the improved ceramic density.

KEYWORDS: *solid electrolytes, lithium garnets, lithium ion conductivity, Li$_7$La$_3$Zr$_2$O$_{12}$*
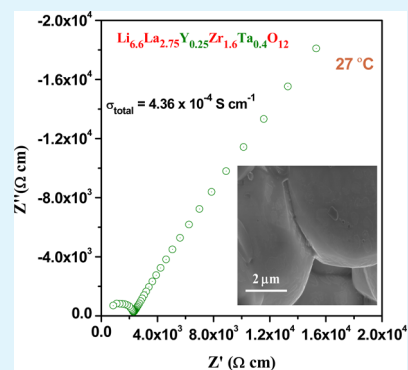
1. INTRODUCTION

Solid-state fast lithium ion (Li$^+$) conductors have attracted much attention in recent times owing to their potential application in electrochemical energy storage devices particularly for developing high performance all-solid-state lithium batteries. Solid Li$^+$ conducting electrolytes are believed to be superior to the presently used organic liquid electrolytes in terms of safety issues such as dendrite formation, flammability, and leakage problems.[1,2] A solid electrolyte with high Li$^+$ conductivity, low electronic conductivity, and a wide electrochemical window is strongly required for the development of safe, high power, and high capacity all solid-state lithium secondary batteries for heavy duty applications like electric vehicle (EV). So far, many inorganic solid electrolytes with different crystal structures including perovskite titanates (Li$_{3x}$La$_{(2/3)-x}$□$_{(1/3)-2x}$TiO$_3$ 0 < x < 0.16),[3–5] NASICON-type (sodium superionic conductors Li$_{1.3}$Ti$_{1.7}$Al$_{0.3}$(PO$_4$)$_3$),[6–8] LISI-

CON-type (lithium superionic conductors Li$_{14}$ZnGe$_4$O$_{16}$),[9,10] and lithium "stuffed" garnets[11–20] have been explored. Among these, garnet-like structural compounds reported by Weppner and his group received considerable attention in recent times for potential application as electrolytes in all-solid-state lithium batteries.[12,13] Particularly, lithium stuffed oxide with the nominal formula Li$_7$La$_3$Zr$_2$O$_{12}$ (LLZ) reported by Murugan et al. has been widely studied because of its high Li$^+$ conductivity (σ_{Li} > 10^{-4} S cm^{-1}) at room temperature and excellent stability against lithium metal anodes.[13,21] LLZ has two different crystal phases: one is the cubic and another is the tetragonal phase.[13,22–24] The LLZ crystal in the tetragonal phase (space group $I4_1/acd$; No. 142) is an ordered structure

with lithium on the tetrahedral $8a$ site and octahedral $16f$ and $32g$ sites.[22] On the other hand the LLZ crystal in the cubic phase (space group $Ia\bar{3}d$; No. 230) is a disordered structure with lithium on tetrahedral $24d$ Li(1) and octahedral $96h$ Li(2) sites.[23] The distorted arrangement of Li$^+$ in cubic phase LLZ compared to complete ordering of Li$^+$ across all of the octahedral and one-third of the tetrahedral in the tetragonal LLZ leads to two orders of higher Li$^+$ conductivity in the cubic phase LLZ.[13,22] However, sintering at high temperature around 1230 °C for 36 h in an alumina crucible is needed to obtain high Li$^+$ conductive cubic LLZ ($Ia\bar{3}d$).[13] Studies suggest that the unintentional incorporation of Al^{3+} from alumina crucibles into the LLZ pellet during the high-temperature solid-state synthesis helps to stabilize the cubic phase ($Ia\bar{3}d$) against the tetragonal one ($I4_1/acd$).[24−26]

The electrochemical investigation on a model battery fabricated using LLZ as the solid electrolyte and LiCoO$_2$ as the cathode revealed poor lithium insertion/extraction at the LLZ/LiCoO$_2$ interface.[27] The interfacial layer formed between LLZ/LiCoO$_2$ during high temperature processing is the major reasons for the poor lithium insertion/extraction at the LLZ/LiCoO$_2$ interface.[27] Suppressing the formation of such an undesirable interfacial layer will be indispensable for developing an all-solid-state rechargeable lithium battery with LLZ as the solid fast lithium ion conductor.

Recent reports revealed that doping with elements such as Al, Nb, Ta, Y, Sr, Sb, Te, Ce, W, Si, Ge, and In could stabilize the LLZ garnet in the cubic phase with high Li$^+$ conductivity.[28−42] Thus, searching for proper dopants has become an important topic in understanding the stabilization of LLZ in the cubic phase and enhancing its Li$^+$ conduction properties. In an attempt to increase the Li$^+$ conductivity, researchers have reported success with substitutions on the Zr^{4+} site in LLZ. The substitution of a supervalent cation, either Nb^{5+} or Ta^{5+}, for Zr^{4+} in LLZ stabilizes the cubic phase relatively at lower sintering temperature and also enhances the Li$^+$ conductivity.[29,30,35] The maximized Li$^+$ conductivity with the substitution of Nb^{5+} for Zr^{4+} in LLZ was observed for the composition Li$_{6.75}$La$_3$Zr$_{1.75}$Nb$_{0.25}$O$_{12}$.[29] The electrochemical performance of an all-solid-state lithium battery fabricated using LiCoO$_2$ as the cathode and Li$_{6.75}$La$_3$Zr$_{1.75}$Nb$_{0.25}$O$_{12}$ as the solid electrolyte exhibited good charge−discharge capacities with low interfacial resistance between the cathode and solid electrolyte.[43] However, a recent report on the stability of Nb-doped LLZ, i.e., Li$_{6.75−x}$La$_3$Zr$_{1.75}$Nb$_{0.25}$O$_{12−0.5x}$, indicated the possible reduction of Nb in LLZ in contact with lithium metal.[44] The first-principles density functional theory (DFT) calculation on the electrochemical stability of lithium garnets Li$_x$La$_3$M$_2$O$_{12}$ (M = Ti, Zr, Nb, Ta, Sb, Bi; x = 5 or 7) against lithium metal also indicated that the Ta-containing lithium garnet Li$_5$La$_3$Ta$_2$O$_{12}$ is more nonreactive with Li metal compared to that of Li$_5$La$_3$Nb$_2$O$_{12}$ because of unfavorable thermodynamics.[45] Li et al. indicated that Ta-doped LLZ is stable up to a measured voltage of 5 V vs Li$^+$/Li.[35] Hence there has been considerable attention in recent times on Ta-doped LLZ for potential application as a solid electrolyte membrane in all-solid-state lithium batteries.

In addition to the high Li$^+$ conductivity, the dense microstructure related to grains and grain boundaries is also a critical issue for the successful application of LLZ as a solid electrolyte membrane in all-solid-state lithium and lithium−air battery applications. The dense microstructure is expected to enhance the total (bulk + grain boundary) Li$^+$ conductivity by

reducing the grain-boundary resistance and also expected to cordon the dendritic growth during lithium deposition. Although the conductivity has been improved by stabilizing the cubic phase relatively at lower sintering temperature with the Ta^{5+} doping for Zr^{4+} in LLZ, the density of the prepared pellet was found to be relatively poor with a large amount of pores compared to dense LLZ.[46,47] The results reported in the literature on doping with LLZ indicated a reduction in sintering temperature with La^{3+} site doping (Sr^{2+} or Ce^{4+})[37,40] and improved conductivity by doping the Zr^{4+} site (Nb^{5+} or Ta^{5+}).[29,31,35] However, there are only a few reports regarding the simultaneous substitution on the La^{3+} and on the Zr^{4+} site in LLZ.[48,49] Therefore, it is vital to explore a new possible sintering agent as dopants to realize the stabilization of cubic phase lithium garnets with dense microstructure and high Li$^+$ conductivity. Y$_2$O$_3$ is also a well-known sintering agent, and hence the small doping of Y^{3+} for La^{3+} in LLZTO is expected to enhance the density.

Investigations on the ionic conductivity of cubic Li$_{7−x}$La$_3$Zr$_{2−x}$Ta$_x$O$_{12}$ indicated that the maximized Li$^+$ conductivity was exhibited for compositions around x = 0.5 ± 0.1.[35] Therefore, we have chosen the high Li$^+$ conductive nominal composition Li$_{6.6}$La$_3$Zr$_{1.6}$Ta$_{0.4}$O$_{12}$ (LLZTO) for further investigation on the effect of doping Y^{3+} for La^{3+} in LLZTO ceramics without altering the optimized lithium content of 6.6. In the present study, systematic investigations have been carried out on Li$_{7−x}$La$_{3−y}$Y$_y$Zr$_{2−x}$Ta$_x$O$_{12}$ (x = 0.4, y = 0, 0.125, 0.25, and 0.5) to understand the effect of substitution of Y^{3+} for La^{3+} and Ta^{5+} for Zr^{4+} in LLZ on the stabilization of the cubic phase, microstructure, and Li$^+$ conduction behavior.

2. EXPERIMENTAL SECTION

A conventional solid-state reaction procedure was employed for the preparation of compounds having nominal compositions Li$_{7−x}$La$_{3−y}$Y$_y$Zr$_{2−x}$Ta$_x$O$_{12}$ (x = 0.4, y = 0, 0.125, 0.25, and 0.5), i.e., Li$_{6.6}$La$_3$Zr$_{1.6}$Ta$_{0.4}$O$_{12}$, Li$_{6.6}$La$_{2.875}$Y$_{0.125}$Zr$_{1.6}$Ta$_{0.4}$O$_{12}$, Li$_{6.6}$La$_{2.75}$Y$_{0.25}$Zr$_{1.6}$Ta$_{0.4}$O$_{12}$, and Li$_{6.6}$La$_{2.5}$Y$_{0.5}$Zr$_{1.6}$Ta$_{0.4}$O$_{12}$, using stoichiometric amounts of high purity chemicals LiNO$_3$ (Sigma-Aldrich, >99%; 15 wt % excess was added to compensate the loss of lithium during sintering), La$_2$O$_3$ (Merck, >99% predried at 900 °C for 24 h), ZrO$_2$ (Acros, 98%), Y$_2$O$_3$ (Sigma-Aldrich, 98%), and Ta$_2$O$_5$ (Alfa-aesar, 99%). The precursors were ball milled with 5 mm diameter zirconia balls in 2-propanol at 300 rpm for about 6 h using a Pulverisette 7, Fritsch, Germany. After the evaporation of the solvents at room temperature, the mixtures were heated from room temperature to 750 °C in an open alumina crucible and held at this temperature for 6 h and then cooled to room temperature. The resultant powders were ground again for 6 h using zirconia balls in 2-propanol. After the evaporation of the solvents the powders were pressed into pellets by uniaxial pressure. The pellets were covered with the same mother powder to reduce possible lithium loss and sintered at 750 °C for 12 h and 1200 °C for 18 h using an alumina crucible. Li$_7$La$_3$Zr$_2$O$_{12}$ (LLZ) in the cubic[13] and tetragonal phase[22] was also prepared at elevated temperature through solid-state reaction with a procedure described earlier for the purpose of comparison.

The sintered pellets were ground into powder for powder X-ray diffraction (PXRD) and Raman measurements. The phase purity and crystal structure of the prepared samples were examined by powder X-ray diffraction (PXRD) using an X'pert PANalytical X-ray diffractometer with Cu−K$_\alpha$ radiation of λ =

1.5418 Å from $2\theta = 10$ to $80°$ with a step width of $0.02°$. A field-emission scanning electron microscope SU8000 Family Ultra-High Resolution (FE-SEM) equipped with an energy-dispersive X-ray detector (EDX) was used to obtain the microstructure of the fractured surface of the pellet. The elemental analysis for the prepared samples was carried out using a wavelength-dispersive X-ray fluorescence spectrometer (WD-XRF), Bruker S4 Pioneer, to estimate the amount of inclusion of Al^{3+} from the alumina crucible. The relative densities of the sintered pellets at room temperature were obtained with the Archimedes principle using deionized water as the immersion medium. Confocal micro-Raman spectra have been recorded at room temperature in the range $50-4000$ cm^{-1} using a Renishaw inVia Reflex spectrometer with a 50 mW internal Ar ion laser source of excitation wavelength 514 nm. Thermogravimetric analysis (TGA) was performed with an SDT Q600 (TA) under air flow with a heating rate of 10 °C/min. Fourier transform infrared (FTIR) spectra were recorded with Thermo Nicolet 6700 using the KBr pellet technique. Electrical conductivity measurements of the prepared pellets were performed using Li^+ blocking Au electrodes (Au paste cured at 600 °C for 1 h) in the temperature range from 27 to 200 °C using a Novocontrol Concept 80 Broadband dielectric spectrometer (BDS).

3. RESULTS AND DISCUSSION

3.1. Powder X-ray diffraction (PXRD).
Figure 1 shows the powder X-ray diffraction (PXRD) patterns of
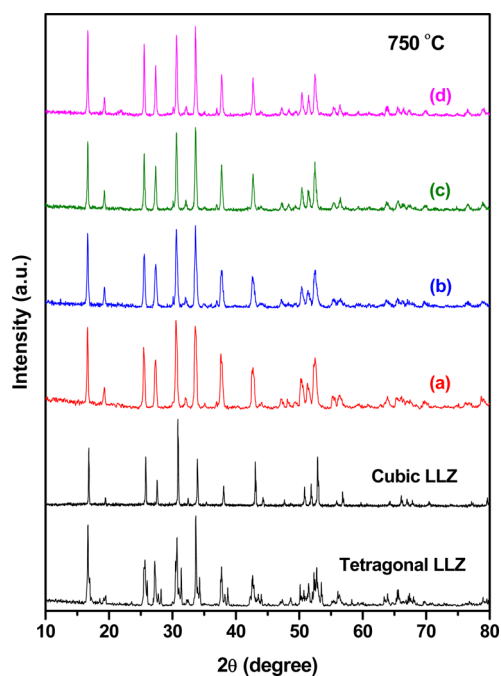
Figure 1. PXRD patterns of (a) $Li_{6.6}La_3Zr_{1.6}Ta_{0.4}O_{12}$, (b) $Li_{6.6}La_{2.875}Y_{0.125}Zr_{1.6}Ta_{0.4}O_{12}$, (c) $Li_{6.6}La_{2.75}Y_{0.25}Zr_{1.6}Ta_{0.4}O_{12}$, and (d) $Li_{6.6}La_{2.5}Y_{0.5}Zr_{1.6}Ta_{0.4}O_{12}$ sintered at 750 °C along with the pattern of tetragonal LLZ and cubic LLZ.

$Li_{6.6}La_3Zr_{1.6}Ta_{0.4}O_{12}$, $Li_{6.6}La_{2.875}Y_{0.125}Zr_{1.6}Ta_{0.4}O_{12}$, $Li_{6.6}La_{2.75}Y_{0.25}Zr_{1.6}Ta_{0.4}O_{12}$, and $Li_{6.6}La_{2.5}Y_{0.5}Zr_{1.6}Ta_{0.4}O_{12}$ sintered at 750 °C along with the patterns of tetragonal LLZ and cubic LLZ. The presence of all the diffraction peaks corresponding to that of the cubic phase and absence of clear

splitting of the diffraction peaks corresponding to that of the characteristic tetragonal phase in the case of the measured PXRD patterns of $Li_{6.6}La_3Zr_{1.6}Ta_{0.4}O_{12}$, $Li_{6.6}La_{2.875}Y_{0.125}Zr_{1.6}Ta_{0.4}O_{12}$, $Li_{6.6}La_{2.75}Y_{0.25}Zr_{1.6}Ta_{0.4}O_{12}$, and $Li_{6.6}La_{2.5}Y_{0.5}Zr_{1.6}Ta_{0.4}O_{12}$ as shown in Figure 1(a–d) indicates the possibility of stabilization of a cubic-like garnet phase even at lower sintering temperature at around 750 °C.

The PXRD patterns of $Li_{6.6}La_3Zr_{1.6}Ta_{0.4}O_{12}$, $Li_{6.6}La_{2.875}Y_{0.125}Zr_{1.6}Ta_{0.4}O_{12}$, $Li_{6.6}La_{2.75}Y_{0.25}Zr_{1.6}Ta_{0.4}O_{12}$, and $Li_{6.6}La_{2.5}Y_{0.5}Zr_{1.6}Ta_{0.4}O_{12}$ sintered at 1200 °C along with the pattern of tetragonal LLZ and cubic LLZ are shown as Figure 2.
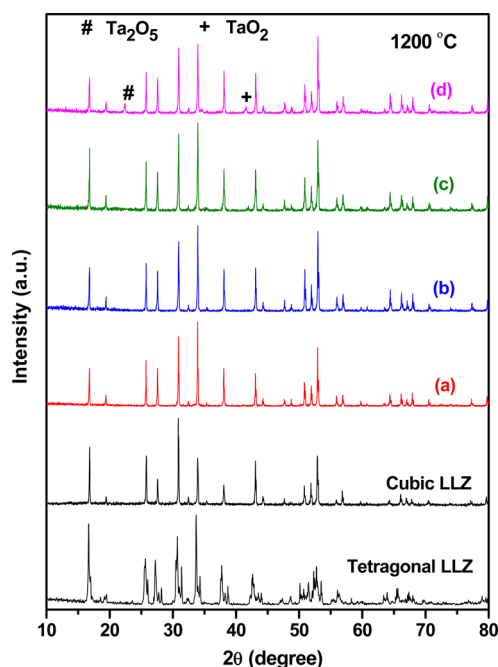

Figure 2. PXRD patterns of (a) $Li_{6.6}La_3Zr_{1.6}Ta_{0.4}O_{12}$, (b) $Li_{6.6}La_{2.875}Y_{0.125}Zr_{1.6}Ta_{0.4}O_{12}$, (c) $Li_{6.6}La_{2.75}Y_{0.25}Zr_{1.6}Ta_{0.4}O_{12}$, and (d) $Li_{6.6}La_{2.5}Y_{0.5}Zr_{1.6}Ta_{0.4}O_{12}$ sintered at 1200 °C along with the pattern of tetragonal LLZ and cubic LLZ.

The PXRD patterns of $Li_{6.6}La_3Zr_{1.6}Ta_{0.4}O_{12}$, $Li_{6.6}La_{2.875}Y_{0.125}Zr_{1.6}Ta_{0.4}O_{12}$, $Li_{6.6}La_{2.75}Y_{0.25}Zr_{1.6}Ta_{0.4}O_{12}$, and $Li_{6.6}La_{2.5}Y_{0.5}Zr_{1.6}Ta_{0.4}O_{12}$ shown in Figure 2(a–d) confirm the garnet-like structure with cubic symmetry, which could be evidenced by sharp diffraction peaks without splitting. Lithium garnet prepared with the nominal composition $Li_{6.6}La_{2.5}Y_{0.5}Zr_{1.6}Ta_{0.4}O_{12}$ exhibits weak impurity peaks corresponding to Ta_2O_5 and TaO_2. The cubic lattice constants of $Li_{6.6}La_3Zr_{1.6}Ta_{0.4}O_{12}$, $Li_{6.6}La_{2.875}Y_{0.125}Zr_{1.6}Ta_{0.4}O_{12}$, $Li_{6.6}La_{2.75}Y_{0.25}Zr_{1.6}Ta_{0.4}O_{12}$, and $Li_{6.6}La_{2.5}Y_{0.5}Zr_{1.6}Ta_{0.4}O_{12}$ sintered at 1200 °C were found to be 12.9484(2), 12.9371(2), 12.9214(1), and 12.9041(3) Å, respectively. The cubic lattice constant decreases nearly linearly with increasing Y substitution since the ionic size of Y^{3+} (0.9 Å) is smaller than that of La^{3+} (1.16 Å).[50]

The selected PXRD patterns ($2\theta = 24$ to $45°$) of $Li_{6.6}La_3Zr_{1.6}Ta_{0.4}O_{12}$, $Li_{6.6}La_{2.875}Y_{0.125}Zr_{1.6}Ta_{0.4}O_{12}$, $Li_{6.6}La_{2.75}Y_{0.25}Zr_{1.6}Ta_{0.4}O_{12}$, and $Li_{6.6}La_{2.5}Y_{0.5}Zr_{1.6}Ta_{0.4}O_{12}$ sintered at 750 and 1200 °C shown as Figure 3 do not exhibit a major change in the pattern but exhibit slightly broadened diffraction peaks along with a clear shift in peak positions toward the lower diffraction angle for the samples sintered at 750 °C compared to that of samples sintered at 1200 °C. The
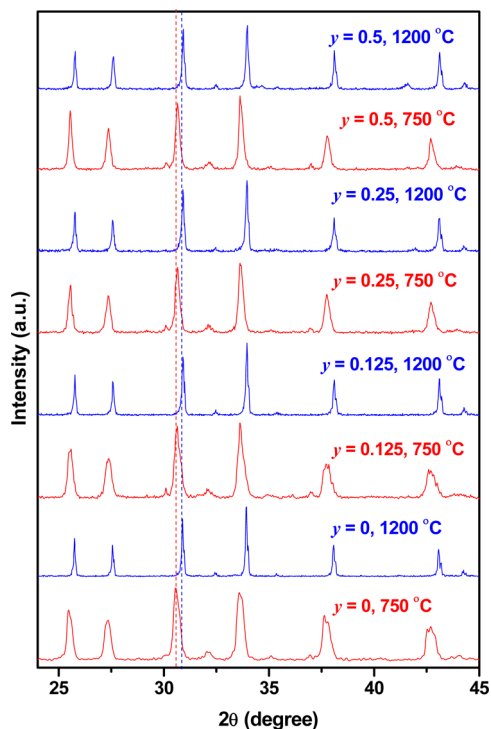
Figure 3. PXRD patterns of (a) $Li_{6.6}La_3Zr_{1.6}Ta_{0.4}O_{12}$, (b) $Li_{6.6}La_{2.875}Y_{0.125}Zr_{1.6}Ta_{0.4}O_{12}$, (c) $Li_{6.6}La_{2.75}Y_{0.25}Zr_{1.6}Ta_{0.4}O_{12}$, and (d) $Li_{6.6}La_{2.5}Y_{0.5}Zr_{1.6}Ta_{0.4}O_{12}$ sintered at 750 °C (red color) and 1200 °C (blue color) in the 2θ range 24 to 45°.

shift in the diffraction peaks toward the lower diffraction angle suggests an increase in the lattice parameter for the samples sintered at 750 °C. The cubic lattice constants of $Li_{6.6}La_3Zr_{1.6}Ta_{0.4}O_{12}$, $Li_{6.6}La_{2.875}Y_{0.125}Zr_{1.6}Ta_{0.4}O_{12}$, $Li_{6.6}La_{2.75}Y_{0.25}Zr_{1.6}Ta_{0.4}O_{12}$, and $Li_{6.6}La_{2.5}Y_{0.5}Zr_{1.6}Ta_{0.4}O_{12}$ sintered at 750 °C were found to be 12.9594(2), 12.9572(4), 12.9506(5), and 12.9479(3) Å, respectively.

3.2. Raman Spectroscopic Studies. Raman scattering is a very powerful technique for acquiring useful information on the structure of ceramic oxides. The Raman spectra of $Li_{6.6}La_3Zr_{1.6}Ta_{0.4}O_{12}$, $Li_{6.6}La_{2.875}Y_{0.125}Zr_{1.6}Ta_{0.4}O_{12}$, $Li_{6.6}La_{2.75}Y_{0.25}Zr_{1.6}Ta_{0.4}O_{12}$, and $Li_{6.6}La_{2.5}Y_{0.5}Zr_{1.6}Ta_{0.4}O_{12}$ sintered at 750 and 1200 °C along with the tetragonal LLZ and cubic LLZ are shown as Figures 4 and 5, respectively. Although the PXRD patterns of $Li_{6.6}La_3Zr_{1.6}Ta_{0.4}O_{12}$, $Li_{6.6}La_{2.875}Y_{0.125}Zr_{1.6}Ta_{0.4}O_{12}$, $Li_{6.6}La_{2.75}Y_{0.25}Zr_{1.6}Ta_{0.4}O_{12}$, and $Li_{6.6}La_{2.5}Y_{0.5}Zr_{1.6}Ta_{0.4}O_{12}$ sintered at 750 and 1200 °C shown as Figures 1 and 2 do not exhibit a major change in the pattern their corresponding Raman spectra shown as Figures 4 and 5 exhibit dramatic differences.

Earlier Raman studies on lithium garnets and related system suggested that the Raman bands for the investigated lithium garnets observed between 100 and 150 cm^{-1} correspond to vibration of the heavy La cation, and the band observed at about 640 cm^{-1} corresponds to the Zr−O bond stretching and the band at around 750 cm^{-1} to the Ta−O bond stretching, respectively.[51,52] For several lithium metal oxide materials and lithium garnets it has been demonstrated that the internal modes of LiO_6 appear in the range 200−300 cm^{-1}, whereas the internal modes of LiO_4 occur in the range 350−500 cm^{-1}.[53,54] Because of the complex nature of the structure of lithium garnets, considerable mixing between internal modes of LiO_4, LiO_6, and the other coordinated groups present in the structure
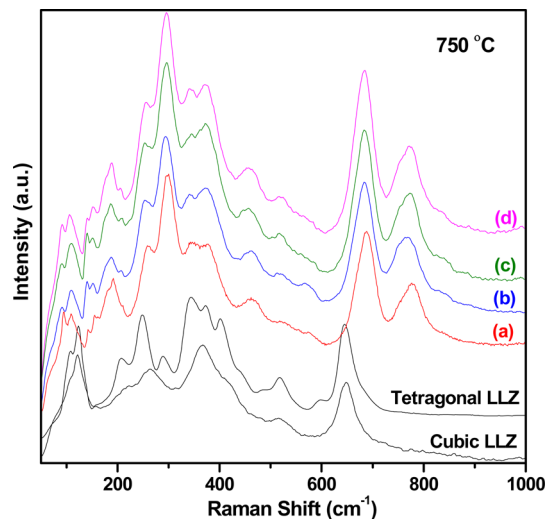

Figure 4. Raman spectra of (a) $Li_{6.6}La_3Zr_{1.6}Ta_{0.4}O_{12}$, (b) $Li_{6.6}La_{2.875}Y_{0.125}Zr_{1.6}Ta_{0.4}O_{12}$, (c) $Li_{6.6}La_{2.75}Y_{0.25}Zr_{1.6}Ta_{0.4}O_{12}$, and (d) $Li_{6.6}La_{2.5}Y_{0.5}Zr_{1.6}Ta_{0.4}O_{12}$ sintered at 750 °C measured in the range 50−1000 cm^{-1} along with the pattern of cubic LLZ and tetragonal LLZ.

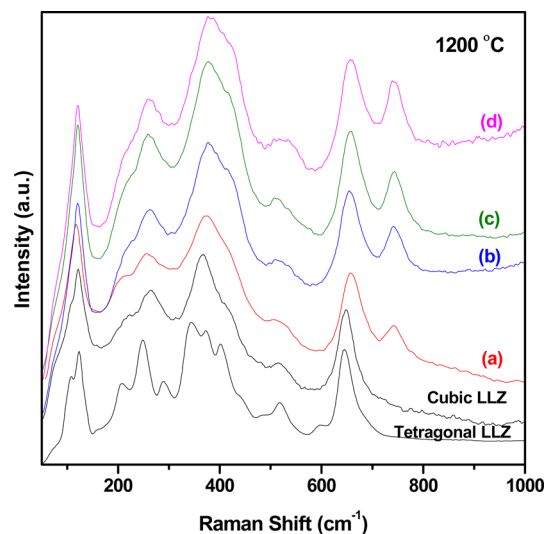**Figure 5.** Raman spectra of (a) $Li_{6.6}La_3Zr_{1.6}Ta_{0.4}O_{12}$, (b) $Li_{6.6}La_{2.875}Y_{0.125}Zr_{1.6}Ta_{0.4}O_{12}$, (c) $Li_{6.6}La_{2.75}Y_{0.25}Zr_{1.6}Ta_{0.4}O_{12}$, and d) $Li_{6.6}La_{2.5}Y_{0.5}Zr_{1.6}Ta_{0.4}O_{12}$ sintered at 1200 °C measured in the range 50−1000 cm^{-1} along with the pattern of cubic LLZ and tetragonal LLZ.

is expected, and thus the interpretation of Raman spectra of lithium garnets becomes much more complicated. Hence it is very difficult to assign the observed Raman bands in the region 200−500 cm^{-1}.

The major difference observed between the Raman spectra of the cubic ($Ia\bar{3}d$) and tetragonal ($I4_1/acd$) phase of LLZ is the presence of a larger number of Raman peaks or bands for tetragonal than that of the cubic phase particularly in the region 200−500 cm^{-1}. The broad spectral features of the cubic garnet in the region 200−500 cm^{-1} might be due to the static or dynamic disorder of highly mobile Li$^+$ compared to the ordered arrangement in the tetragonal phase.[55] The Raman spectrum in the intermediate-energy region of cubic LLZ exhibits a few broad and fairly overlapping bands associated with degenerate Raman modes, which turn out partly split in the tetragonal LLZ

phase, due to its lower symmetry, thus originating a higher number of observed peaks. The weak intense band at 209 cm^{-1}, strong peak at 248 cm^{-1}, medium strong peak at 291 cm^{-1}, and strong intense peak at 346, 370, and 404 cm^{-1} are the characteristic Raman peaks observed for tetragonal LLZ. The medium intense broad band at 263 cm^{-1}, medium strong broad band at 366 cm^{-1}, and medium broad shoulder at 417 cm^{-1} are the characteristic Raman bands observed for the cubic LLZ.

The Raman bands observed in the range 200−500 cm^{-1} (Figures 4 and 5) corresponding to the expected internal modes of LiO$_4$ and LiO$_6$ clearly revealed the major difference between the samples sintered at 750 and 1200 °C. The Raman spectra of Li$_{6.6}$La$_3$Zr$_{1.6}$Ta$_{0.4}$O$_{12}$, Li$_{6.6}$La$_{2.875}$Y$_{0.125}$Zr$_{1.6}$Ta$_{0.4}$O$_{12}$, Li$_{6.6}$La$_{2.75}$Y$_{0.25}$Zr$_{1.6}$Ta$_{0.4}$O$_{12}$, and Li$_{6.6}$La$_{2.5}$Y$_{0.5}$Zr$_{1.6}$Ta$_{0.4}$O$_{12}$ sintered at 750 °C measured in the range 200−500 cm^{-1} revealed at least six bands with a maximum intense band at around 295 cm^{-1}, medium intense bands at around 255, 342, 371, and 462 cm^{-1}, and a weak band at around 206 cm^{-1}. The Raman spectra of Li$_{6.6}$La$_3$Zr$_{1.6}$Ta$_{0.4}$O$_{12}$, Li$_{6.6}$La$_{2.875}$Y$_{0.125}$Zr$_{1.6}$Ta$_{0.4}$O$_{12}$, Li$_{6.6}$La$_{2.75}$Y$_{0.25}$Zr$_{1.6}$Ta$_{0.4}$O$_{12}$, and Li$_{6.6}$La$_{2.5}$Y$_{0.5}$Zr$_{1.6}$Ta$_{0.4}$O$_{12}$ sintered at 1200 °C measured in the range 200−500 cm^{-1} revealed a broad intense band at around 377 cm^{-1}, broad medium intense band at around 260 cm^{-1}, and shoulder band at around 420 cm^{-1}. The close observation between the Raman spectra shown in Figures 4 and 5 revealed that the phase stabilized at around 750 °C for the Li$_{7-x}$La$_{3-y}$Y$_y$Zr$_{2-x}$Ta$_x$O$_{12}$ (x = 0.4, y = 0, 0.125, 0.25, and 0.5) sample is different from that of both the tetragonal ($I4_1/acd$) and high Li$^+$ conductive cubic phase ($Ia\bar{3}d$), and the transformation to the high Li$^+$ conductive cubic phase with distorted lithium sublattice ($Ia\bar{3}d$) is observed for the samples sintered at elevated temperature around 1200 °C.

In addition to the above difference in the Raman spectra of Li$_{6.6}$La$_3$Zr$_{1.6}$Ta$_{0.4}$O$_{12}$, Li$_{6.6}$La$_3$Zr$_{1.6}$Ta$_{0.4}$O$_{12}$, Li$_{6.6}$La$_{2.875}$Y$_{0.125}$Zr$_{1.6}$Ta$_{0.4}$O$_{12}$, Li$_{6.6}$La$_{2.75}$Y$_{0.25}$Zr$_{1.6}$Ta$_{0.4}$O$_{12}$, and Li$_{6.6}$La$_{2.5}$Y$_{0.5}$Zr$_{1.6}$Ta$_{0.4}$O$_{12}$ sintered at 750 and 1200 °C, an appreciable shift in the positions of vibrational stretching modes of ZrO$_6$ and TaO$_6$ octahedral units was observed as shown in Figure 6. The Raman spectrum of Li$_{6.6}$La$_{2.75}$Y$_{0.25}$Zr$_{1.6}$Ta$_{0.4}$O$_{12}$ exhibits a shift of Zr−O stretching mode from 684 to 656 cm^{-1} and Ta−O stretching mode from 773 to 743 cm^{-1}, while sintering temperature increased from 750 to 1200 °C. A similar shift in the Zr−O and Ta−O stretching mode was observed for the remaining samples as shown in Figure 6. The shift of approximately 30 cm^{-1} toward lower wavenumber observed for the Zr−O and Ta−O stretching modes and broadening of the Raman bands in the intermediate energy range clearly revealed an appreciable modifications in the crystal structure for the Li$_{6.6}$La$_3$Zr$_{1.6}$Ta$_{0.4}$O$_{12}$, Li$_{6.6}$La$_{2.875}$Y$_{0.125}$Zr$_{1.6}$Ta$_{0.4}$O$_{12}$, Li$_{6.6}$La$_{2.75}$Y$_{0.25}$Zr$_{1.6}$Ta$_{0.4}$O$_{12}$, and Li$_{6.6}$La$_{2.5}$Y$_{0.5}$Zr$_{1.6}$Ta$_{0.4}$O$_{12}$ samples, while sintering temperature increased from 750 to 1200 °C.

Investigation on the structural stability of tetragonal phase LLZ by Wang et al. revealed the tetragonal to cubic phase transition around 100−150 °C and cubic to tetragonal phase transition around 800−900 °C.[56] The tetragonal phase or lithium-deficient lithium garnets were reported to be sensitive to humid conditions.[51] The formation of a low temperature cubic phase well below the usual tetragonal to cubic transition temperature is found to depend upon hydration mechanisms.[51] The nature of the high and low temperature cubic garnets is totally different: the one found above the phase transition
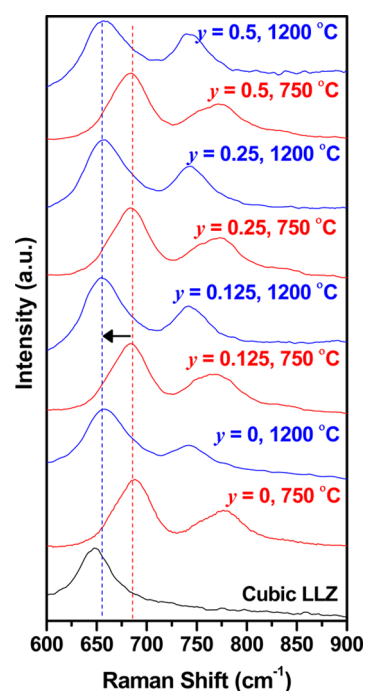

Figure 6. Raman spectra of Li$_{7-x}$La$_{3-y}$Y$_y$Zr$_{2-x}$Ta$_x$O$_{12}$ (x = 0.4, y = 0, 0.125, 0.25, and 0.5) sintered at 750 °C (red color) and 1200 °C (blue color) along with the pattern of cubic LLZ (black color) measured in the range 600−900 cm^{-1} showing an appreciable shift in the positions of vibrational stretching modes of ZrO$_6$ and TaO$_6$ octahedral units.

(tetragonal to cubic) at higher temperature does not involve any major change in the stoichiometry, whereas the cubic phase formed at low temperature might be due to the effect of the insertion of water molecules and the protonation through the H$^+$/Li$^+$ exchange mechanism into the garnet structure.

Thermogravimetric (TG), Raman, and FTIR measurements for samples sintered at 750 °C were carried out to investigate the hydration effect in these samples. Raman spectra revealed the presence of OH stretching vibration around 3537 cm^{-1} shown as Figure S1 (see Supporting Information). Similarly the FTIR spectra (Figure S2, Supporting Information) revealed the presence of OH stretching vibration at around 3567 cm^{-1}. TG thermograms of all these samples indicated the onset of major weight loss around 300 °C and ends at 450 °C shown in Figure S3 (see Supporting Information). In addition to this an additional small weight loss in the temperature range 200−300 °C is observed for the Li$_{7-x}$La$_{3-y}$Y$_y$Zr$_{2-x}$Ta$_x$O$_{12}$ (x = 0.4, y = 0) sample only. The major weight loss observed at around 300−450 °C in TG might be due to the release of crystalline water and not from the surface adsorbed water. The water vapor from the atmosphere might enter into the lattice and replaced the lithium ions by protons to form O−H bonds.[57] An increase in the cell parameter observed for the Li$_{6.6}$La$_3$Zr$_{1.6}$Ta$_{0.4}$O$_{12}$, Li$_{6.6}$La$_{2.875}$Y$_{0.125}$Zr$_{1.6}$Ta$_{0.4}$O$_{12}$, Li$_{6.6}$La$_{2.75}$Y$_{0.25}$Zr$_{1.6}$Ta$_{0.4}$O$_{12}$, and Li$_{6.6}$La$_{2.5}$Y$_{0.5}$Zr$_{1.6}$Ta$_{0.4}$O$_{12}$ sintered at 750 °C compared to that of 1200 °C might be due to the replacement of Li−O bonds by O−H···O hydrogen bonds.[58] The changes in the Raman spectra revealed that the cubic-like phase observed for the Li$_{6.6}$La$_3$Zr$_{1.6}$Ta$_{0.4}$O$_{12}$, Li$_{6.6}$La$_{2.875}$Y$_{0.125}$Zr$_{1.6}$Ta$_{0.4}$O$_{12}$, Li$_{6.6}$La$_{2.75}$Y$_{0.25}$Zr$_{1.6}$Ta$_{0.4}$O$_{12}$, and Li$_{6.6}$La$_{2.5}$Y$_{0.5}$Zr$_{1.6}$Ta$_{0.4}$O$_{12}$ samples sintered at 750 °C is different from the $Ia\bar{3}d$ space group cubic phase. However, further detailed temperature-dependent

Raman, neutron, and nuclear magnetic resonance (NMR) investigations are essential for unambiguous understanding.

3.3. Microstructural Analysis. A dense polycrystalline ceramic electrolyte with large size grain is highly desired for device application. High porosity in solid electrolytes may cause a high grain boundary resistance as well as mechanical failure. Particularly for all-solid-state lithium battery application solid electrolytes with a dense microstructure are very much essential to avoid dendritic growth during lithium deposition. FE-SEM images of the fractured surface of $Li_{6.6}La_3Zr_{1.6}Ta_{0.4}O_{12}$, $Li_{6.6}La_{2.875}Y_{0.125}Zr_{1.6}Ta_{0.4}O_{12}$, $Li_{6.6}La_{2.75}Y_{0.25}Zr_{1.6}Ta_{0.4}O_{12}$, and $Li_{6.6}La_{2.5}Y_{0.5}Zr_{1.6}Ta_{0.4}O_{12}$ pellets sintered at 1200 °C are shown in Figure 7(a−h). The magnified FE-SEM images of these pellets are shown as Figure 7(e−h). The cross-sectional FE-SEM images performed on a larger area (20 μm) of the
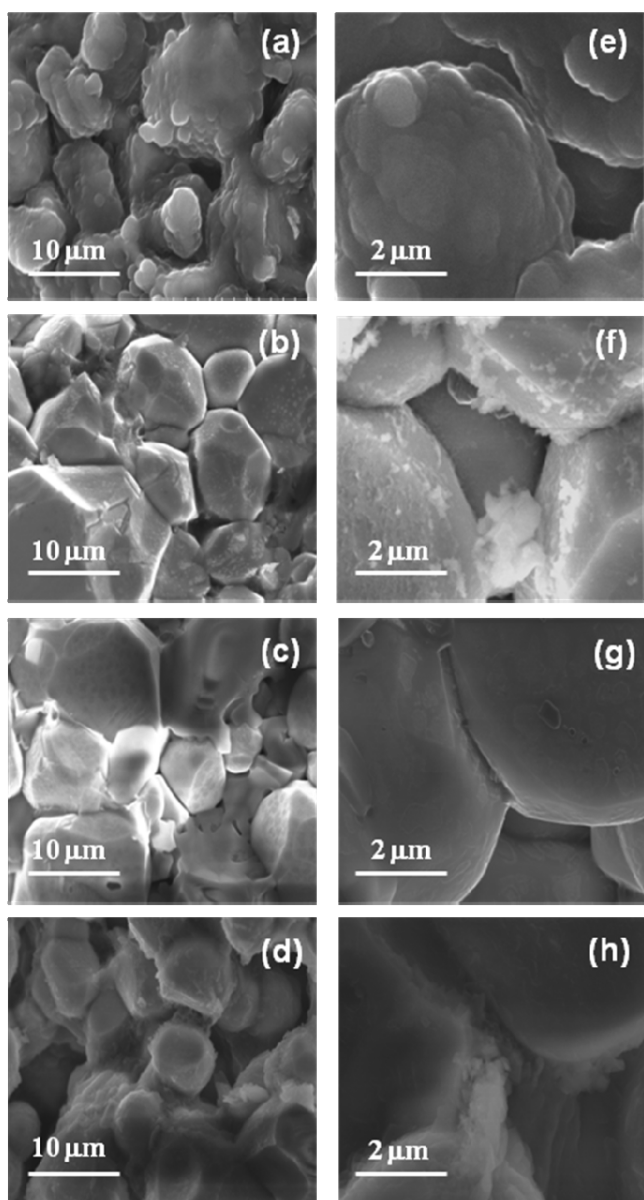
Figure 7. FE-SEM images of the fractured surface of (a) $Li_{6.6}La_3Zr_{1.6}Ta_{0.4}O_{12}$, (b) $Li_{6.6}La_{2.875}Y_{0.125}Zr_{1.6}Ta_{0.4}O_{12}$, (c) $Li_{6.6}La_{2.75}Y_{0.25}Zr_{1.6}Ta_{0.4}O_{12}$, and (d) $Li_{6.6}La_{2.5}Y_{0.5}Zr_{1.6}Ta_{0.4}O_{12}$ samples sintered at 1200 °C and (e−h) represent the magnified FE-SEM images of the respective samples.

$Li_{6.6}La_3Zr_{1.6}Ta_{0.4}O_{12}$ and Y-substituted relatively dense $Li_{6.6}La_{2.75}Y_{0.25}Zr_{1.6}Ta_{0.4}O_{12}$ samples are provided as Figure S4 in the Supporting Information.

FE-SEM images of $Li_{6.6}La_3Zr_{1.6}Ta_{0.4}O_{12}$ (Figure 7(a and e)) reveal the absence of well-crystallized grains and the appearance of pores in between the grains, which lead to poor density. By introduction of yttrium as a dopant a significant change in microstructure has been observed as shown in Figure 7(b−d, f−h) and Figure S4 (Supporting Information). At low yttrium concentration, the FE-SEM images of $Li_{6.6}La_{2.875}Y_{0.125}Zr_{1.6}Ta_{0.4}O_{12}$ as shown in Figure 7(b and f) reveal the growth of grains and better contact with the neighboring grains, but a certain amount of pores can be observed in between the grains. FE-SEM images of $Li_{6.6}La_{2.75}Y_{0.25}Zr_{1.6}Ta_{0.4}O_{12}$ shown in Figure 7(c and g) and Figure S4 (Supporting Information) reveal well-crystallized large grains, large contact area of the grains with the neighboring grains, reduction in the size of pores at the grain boundaries, and the absence of any visible secondary phase. Good connection between the grains and absence of a secondary phase in the grain boundary are expected to reduce the grain boundary resistance. Further increase of the Y dopant leads to segregation of the secondary phase between the grains of $Li_{6.6}La_{2.5}Y_{0.5}Zr_{1.6}Ta_{0.4}O_{12}$ as shown in Figure 7(d and h). FE-SEM investigations on the investigated samples indicate that the Y dopant also acts as the sintering aid during the preparation process by improving the better connection between grains. The maximized relative density was observed for the $Li_{6.6}La_{2.75}Y_{0.25}Zr_{1.6}Ta_{0.4}O_{12}$ sample as given in Table 1. The theoretical, experimental, and relative density of Y- and Ta-doped LLZ with different Y contents are provided as Table S1 (see Supporting Information for details).

EDX mapping for $Li_{6.6}La_{2.75}Y_{0.25}Zr_{1.6}Ta_{0.4}O_{12}$ and $Li_{6.6}La_{2.5}Y_{0.5}Zr_{1.6}Ta_{0.4}O_{12}$ samples sintered at 1200 °C has been given as Figure S5 and Figure S6, respectively, in the Supporting Information. The elemental mapping for the $Li_{6.6}La_{2.75}Y_{0.25}Zr_{1.6}Ta_{0.4}O_{12}$ shown as Figure S5 revealed the uniform distribution of La, Y, Zr, Al, and Ta throughout the grains and also indicated the absence of any secondary phase at the grain boundary. EDX mapping for the Y-rich sample $Li_{6.6}La_{2.5}Y_{0.5}Zr_{1.6}Ta_{0.4}O_{12}$ (Figure S6) indicated the possible segregation of a Y-containing secondary phase at the grain boundary.

Studies on lithium-containing garnets revealed that unintentional incorporation of Al^{3+} from the crucibles helps to stabilize the high conductive cubic phase. The XRF and EDX studies on the investigated lithium garnets sintered at 750 °C indicated the absence of Al^{3+} in these samples. However, the XRF and EDX studies indicated the inclusion of Al^{3+} from the alumina crucible during the preparation of the investigated lithium garnets at high sintering temperature around 1200 °C. The amount of Al^{3+} content present in the $Li_{6.6}La_3Zr_{1.6}Ta_{0.4}O_{12}$, $Li_{6.6}La_{2.875}Y_{0.125}Zr_{1.6}Ta_{0.4}O_{12}$, $Li_{6.6}La_{2.75}Y_{0.25}Zr_{1.6}Ta_{0.4}O_{12}$, and $Li_{6.6}La_{2.5}Y_{0.5}Zr_{1.6}Ta_{0.4}O_{12}$ sintered at 1200 °C was estimated to be 0.66, 0.57, 0.36, and 0.25 wt %, respectively. The minimum amount of Al^{3+} necessary to stabilize the LLZ sample in the cubic phase was estimated to be around 0.9 wt %.[59] The presence of Al^{3+} content less than the 0.9 wt % in the investigated samples indicated that the stabilization of the cubic phase in this work is not merely by the inclusion of Al^{3+} alone. A recent report also confirmed the stabilization of LLZ in the cubic phase through Ta doping without Al^{3+}.[60]

Table 1. Lattice Parameter, Bulk and Total (Bulk + Grain Boundary) Li⁺ Conductivity, Activation Energy for Total Li⁺ Conductivity (in the Temperature Range 27−200 °C), and Relative Density of $Li_{7-x}La_{3-y}Y_yZr_{2-x}Ta_xO_{12}$ ($x = 0.4$, $y = 0$, 0.125, 0.25, and 0.5) Sintered at 1200 °C

nominal composition	lattice parameter, a (Å)	σ_{bulk} 27 °C (S cm⁻¹)	σ_{total} 27 °C (S cm⁻¹)	E_a (eV)	relative density (%)
$Li_{6.6}La_3Zr_{1.6}Ta_{0.4}O_{12}$	12.9484(2)	3.13×10^{-4}	3.04×10^{-4}	0.38	83
$Li_{6.6}La_{2.875}Y_{0.125}Zr_{1.6}Ta_{0.4}O_{12}$	12.9371(2)	-	3.17×10^{-4}	0.35	85
$Li_{6.6}La_{2.75}Y_{0.25}Zr_{1.6}Ta_{0.4}O_{12}$	12.9214(1)	-	4.36×10^{-4}	0.34	95
$Li_{6.6}La_{2.5}Y_{0.5}Zr_{1.6}Ta_{0.4}O_{12}$	12.9041(3)	3×10^{-4}	2.26×10^{-4}	0.39	90

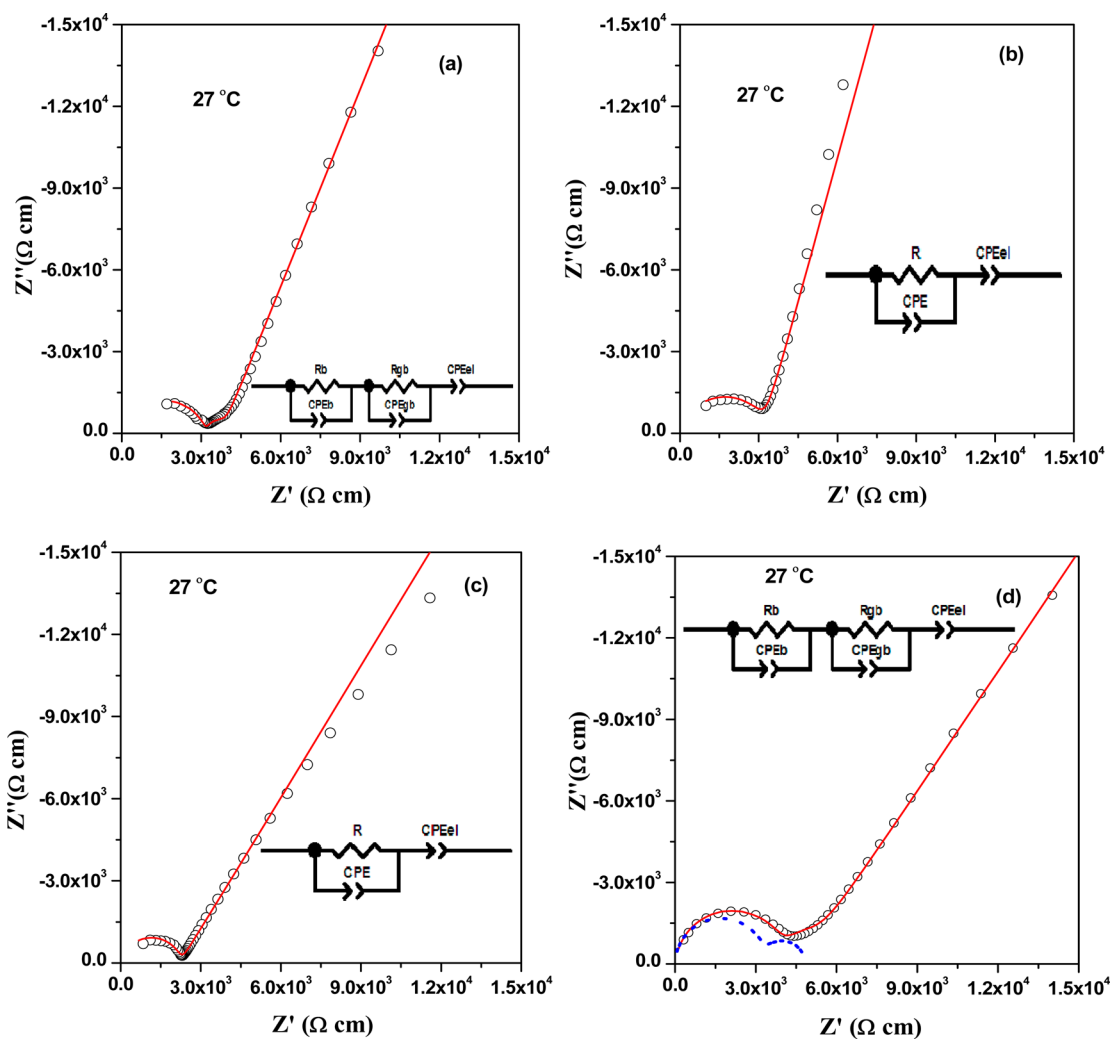**Figure 8.** Typical AC impedance plots measured at room temperature (27 °C) for (a) $Li_{6.6}La_3Zr_{1.6}Ta_{0.4}O_{12}$, (b) $Li_{6.6}La_{2.875}Y_{0.125}Zr_{1.6}Ta_{0.4}O_{12}$, (c) $Li_{6.6}La_{2.75}Y_{0.25}Zr_{1.6}Ta_{0.4}O_{12}$, and (d) $Li_{6.6}La_{2.5}Y_{0.5}Zr_{1.6}Ta_{0.4}O_{12}$ pellets sintered at 1200 °C using Li⁺ blocking Au electrodes. Open circles are the experimental data, and the solid lines are the fitted curves with an equivalent circuit model. The two semicircles (dotted line) below the fitting curve illustrate (d) the separation of bulk and grain boundary contributions, respectively.

3.4. Electrical Properties. Typical AC impedance plots measured at room temperature (27 °C) for $Li_{6.6}La_3Zr_{1.6}Ta_{0.4}O_{12}$, $Li_{6.6}La_{2.875}Y_{0.125}Zr_{1.6}Ta_{0.4}O_{12}$, $Li_{6.6}La_{2.75}Y_{0.25}Zr_{1.6}Ta_{0.4}O_{12}$, and $Li_{6.6}La_{2.5}Y_{0.5}Zr_{1.6}Ta_{0.4}O_{12}$ sintered at 750 °C are shown as Figure S7 (Supporting Information). The total (bulk + grain boundary) conductivity values of all the investigated samples were in the order of 10^{-7} to 10^{-8} S cm⁻¹ (see Table S2 in Supporting Information). Typical AC impedance plots measured at room temperature (27 °C) for $Li_{6.6}La_3Zr_{1.6}Ta_{0.4}O_{12}$, $Li_{6.6}La_{2.875}Y_{0.125}Zr_{1.6}Ta_{0.4}O_{12}$, $Li_{6.6}La_{2.75}Y_{0.25}Zr_{1.6}Ta_{0.4}O_{12}$, and $Li_{6.6}La_{2.5}Y_{0.5}Zr_{1.6}Ta_{0.4}O_{12}$ sintered at 1200 °C are shown in Figure 8(a−d). For direct comparison among the samples with different geometrical sizes, the

real and imaginary parts of impedance Z' and Z'' are multiplied by a factor of A/t (Figure 8(a−d)), where A and t are surface area and thickness of each pellet, respectively. The appearance of a low frequency tail in the case of an ionically blocking Au electrode is an indication that the investigated material is ionically conductive in nature. Similar behavior has been observed for most of the reported high Li⁺ conductive lithium garnets.[13,14,36]

The AC impedance data of $Li_{6.6}La_3Zr_{1.6}Ta_{0.4}O_{12}$ (Figure 8(a)) were fitted with a suitable equivalent circuit using individual resistances and constant phase elements (CPEs) representing the electrical bulk, grain boundary, and electrode response, respectively, (R_bCPE_b) $(R_{gb}CPE_{gb})$ (CPE_{el}) (where R

is the resistance and CPE is the constant phase element and the subscripts b and gb and el refer to the bulk, grain boundary, and electrode contribution, respectively). The bulk and total (bulk + grain boundary) Li$^+$ conductivity of Li$_{6.6}$La$_3$Zr$_{1.6}$Ta$_{0.4}$O$_{12}$ were estimated to be 3.13×10^{-4} and 3.04×10^{-4} S cm^{-1}, respectively. The AC impedance plots for the Li$_{6.6}$La$_{2.875}$Y$_{0.125}$Zr$_{1.6}$Ta$_{0.4}$O$_{12}$ and Li$_{6.6}$La$_{2.75}$Y$_{0.25}$Zr$_{1.6}$Ta$_{0.4}$O$_{12}$ shown as Figure 8(b and c) revealed that the bulk and grain boundary contributions could not be resolved clearly which in turn indicates negligible grain boundary resistance in that sample. Hence, the corresponding impedance plots were fitted with the suitable equivalent circuit using individual resistances and a constant phase element (CPE) representing the total resistance and electrode response, respectively, (RCPE) (CPE$_{el}$). The total Li$^+$ conductivity for Li$_{6.6}$La$_{2.875}$Y$_{0.125}$Zr$_{1.6}$Ta$_{0.4}$O$_{12}$ and Li$_{6.6}$La$_{2.75}$Y$_{0.25}$Zr$_{1.6}$Ta$_{0.4}$O$_{12}$ was estimated to be 3.17×10^{-4} and 4.36×10^{-4} S cm^{-1}, respectively. The experimental impedance data points of Li$_{6.6}$La$_{2.5}$Y$_{0.5}$Zr$_{1.6}$Ta$_{0.4}$O$_{12}$ were fitted with a suitable equivalent circuit using individual resistances and constant phase elements (CPEs) representing the electrical bulk, grain boundary, and electrode response, respectively, (R$_b$CPE$_b$) (R$_{gb}$CPE$_{gb}$) (CPE$_{el}$) (Figure 8(d)). The bulk and total (bulk + grain boundary) Li$^+$ conductivity of Li$_{6.6}$La$_{2.5}$Y$_{0.5}$Zr$_{1.6}$Ta$_{0.4}$O$_{12}$ were estimated to be 3×10^{-4} and 2.26×10^{-4} S cm^{-1}, respectively.

Arrhenius plots for the total (bulk + grain boundary) Li$^+$ ionic conductivity of garnet structured electrolytes Li$_{6.6}$La$_3$Zr$_{1.6}$Ta$_{0.4}$O$_{12}$, Li$_{6.6}$La$_{2.875}$Y$_{0.125}$Zr$_{1.6}$Ta$_{0.4}$O$_{12}$, Li$_{6.6}$La$_{2.75}$Y$_{0.25}$Zr$_{1.6}$Ta$_{0.4}$O$_{12}$, and Li$_{6.6}$La$_{2.5}$Y$_{0.5}$Zr$_{1.6}$Ta$_{0.4}$O$_{12}$ are shown in Figure 9. Arrhenius plots shown in Figure 9 indicated
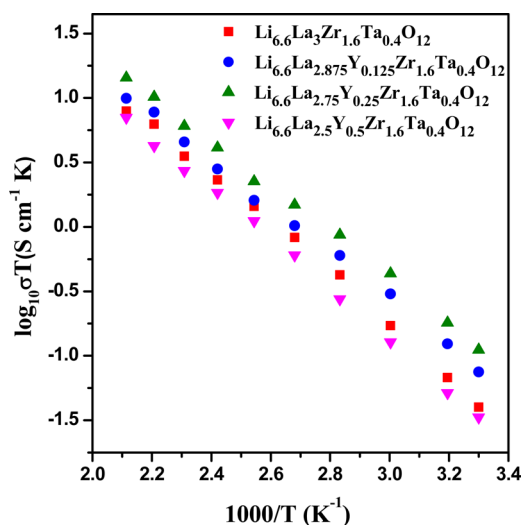
Figure 9. Arrhenius plot of Li$_{6.6}$La$_3$Zr$_{1.6}$Ta$_{0.4}$O$_{12}$, Li$_{6.6}$La$_{2.875}$Y$_{0.125}$Zr$_{1.6}$Ta$_{0.4}$O$_{12}$, Li$_{6.6}$La$_{2.75}$Y$_{0.25}$Zr$_{1.6}$Ta$_{0.4}$O$_{12}$, and Li$_{6.6}$La$_{2.5}$Y$_{0.5}$Zr$_{1.6}$Ta$_{0.4}$O$_{12}$ measured in the temperature range from 27 to 200 °C.

that the investigated samples are thermally stable without any phase transition since there is no appreciable shift in conductivity in the temperature range from 27 to 200 °C. The activation energies (E_a) for the ionic conductivity (σ) were determined from the Arrhenius plots employing the equation

$$\sigma T = A \exp\left(\frac{-E_a}{kT}\right) \tag{1}$$

where A is the pre-exponential parameter; k is Boltzmann's constant; and T is the absolute temperature. The activation energy (E_a) can be estimated from the slope of log(σT) vs $1000/T$.

The variation of total Li$^+$ conductivity measured at 27 °C indicated that the total (bulk + grain boundary) Li$^+$ conductivity increased initially with an increase of Y dopant and reached a maximized value of 4.36×10^{-4} S cm^{-1} for Li$_{6.6}$La$_{2.75}$Y$_{0.25}$Zr$_{1.6}$Ta$_{0.4}$O$_{12}$ and then decreases with further increase of the Y dopant, i.e., for Li$_{6.6}$La$_{2.5}$Y$_{0.5}$Zr$_{1.6}$Ta$_{0.4}$O$_{12}$. In contrast, the activation energy (measured in the temperature range from 27 to 200 °C) initially decreases with an increase of Y dopant and reaches a minimum of 0.34 eV for Li$_{6.6}$La$_{2.75}$Y$_{0.25}$Zr$_{1.6}$Ta$_{0.4}$O$_{12}$ and then increases with the further increase of Y dopant, i.e., for Li$_{6.6}$La$_{2.5}$Y$_{0.5}$Zr$_{1.6}$Ta$_{0.4}$O$_{12}$. The enhancement in total (bulk + grain boundary) Li$^+$ conductivity in Li$_{6.6}$La$_{2.75}$Y$_{0.25}$Zr$_{1.6}$Ta$_{0.4}$O$_{12}$ might be related to the dense microstructure as reflected in the FE-SEM image and density measurement. The decrease in the total (bulk + grain boundary) Li$^+$ conductivity for the lithium garnet with nominal composition Li$_{6.6}$La$_{2.5}$Y$_{0.5}$Zr$_{1.6}$Ta$_{0.4}$O$_{12}$ might be due to the formation of a secondary phase as revealed by FE-SEM/EDX images.

The lattice parameter, relative densities of the pellets measured using Archimedes principle, bulk and total (bulk + grain boundary) Li$^+$ conductivity measured at room temperature (27 °C), and activation energies derived from the Arrhenius plot for total Li$^+$ conductivity (in the temperature range from 27 to 200 °C) for the samples sintered at 1200 °C are tabulated in Table 1.

The results obtained in this work indicated that the optimal Y substitution helps to reduce the grain boundary resistance in a major way and also helps to reduce the bulk resistance slightly. AC impedance analysis on the investigated samples indicated that Li$_{6.6}$La$_3$Zr$_{1.6}$Ta$_{0.4}$O$_{12}$ (Figure 8a) and Li$_{6.6}$La$_{2.5}$Y$_{0.5}$Zr$_{1.6}$Ta$_{0.4}$O$_{12}$ (Figure 8d) have detectable grain boundary resistances. However, Li$_{6.6}$La$_{2.875}$Y$_{0.125}$Zr$_{1.6}$Ta$_{0.4}$O$_{12}$ (Figure 8b) and Li$_{6.6}$La$_{2.75}$Y$_{0.25}$Zr$_{1.6}$Ta$_{0.4}$O$_{12}$ (Figure 8c) do not exhibit any resolvable grain boundary resistance. When the Y substitution is lower it helps to reduce the grain boundary resistance, but larger doping of Y (greater than $y = 0.25$ in Li$_{7-x}$La$_{3-y}$Y$_y$Zr$_{2-x}$Ta$_x$O$_{12}$ ($x = 0.4$)) leads to segregation of Y containing secondary phases into the grain boundary and increases the grain boundary resistance. The AC impedance, FESEM/EDX, and density studies indicated that the optimal amount of yttrium incorporation in LLZTO (i.e., Li$_{6.6}$La$_{2.75}$Y$_{0.25}$Zr$_{1.6}$Ta$_{0.4}$O$_{12}$) helps to enhance the total Li$^+$ conductivity along with the dense microstructure.

4. CONCLUSIONS

Garnet-structured solid electrolytes Li$_{6.6}$La$_3$Zr$_{1.6}$Ta$_{0.4}$O$_{12}$, Li$_{6.6}$La$_{2.875}$Y$_{0.125}$Zr$_{1.6}$Ta$_{0.4}$O$_{12}$, Li$_{6.6}$La$_{2.75}$Y$_{0.25}$Zr$_{1.6}$Ta$_{0.4}$O$_{12}$, and Li$_{6.6}$La$_{2.5}$Y$_{0.5}$Zr$_{1.6}$Ta$_{0.4}$O$_{12}$ were prepared by conventional solid-state reaction method. Raman spectra revealed that the cubic phase stabilized at around 750 °C for the Li$_{7-x}$La$_{3-y}$Y$_y$Zr$_{2-x}$Ta$_x$O$_{12}$ ($x = 0.4$, $y = 0$, 0.125, 0.25, and 0.5) sample is different from that of the high Li$^+$ conductive cubic phase ($Ia\overline{3}d$), and the transition to a high Li$^+$ conductive cubic phase with distorted lithium sublattice ($Ia\overline{3}d$) was observed for the samples sintered at elevated temperature around 1200 °C. Thermogravimetric (TG), Raman, and FTIR studies indicated that the cubic phase exhibited by the investigated lithium garnets sintered at 750 °C might be driven by the insertion of

water vapor from the humid atmosphere. The water vapor from the atmosphere might enter into the lattice and replace the lithium ions by protons to form O−H bonds. FE-SEM images revealed that the lithium garnet with nominal composition $Li_{6.6}La_{2.75}Y_{0.25}Zr_{1.6}Ta_{0.4}O_{12}$ is relatively dense, and the grains are in good contact with each other. This could be due to the better sinterability of the garnets with the yttrium doping. Among the investigated lithium garnets, $Li_{6.6}La_{2.75}Y_{0.25}Zr_{1.6}Ta_{0.4}O_{12}$ sintered at 1200 °C exhibits maximized room temperature total (bulk + grain boundary) Li^+ conductivity of 4.36×10^{-4} S cm^{-1}. The present study indicated the possibility of enhancement in the density and total Li^+ conductivity of LLZ through a suitable and optimal amount of dopant for La and Zr along with optimal lithium concentration. The observation of high total (bulk + grain boundary) Li^+ conduction and relatively dense microstructure suggests that this lithium garnet $Li_{6.6}La_{2.75}Y_{0.25}Zr_{1.6}Ta_{0.4}O_{12}$ may be a promising solid ceramic electrolyte for all-solid-state lithium rechargeable batteries.

■ ASSOCIATED CONTENT

Ⓢ Supporting Information

Table showing theoretical and experimental density of the investigated samples and figures showing Raman, FTIR, TGA, FESEM, EDX, and AC impedance plots of 750 °C sintered pellets. This material is available free of charge via the Internet at http://pubs.acs.org.

■ AUTHOR INFORMATION

Corresponding Author
*Phone: 91 413 2654782. E-mail: moranamurugan.phy@pondiuni.edu.in.

Notes
The authors declare no competing financial interest.

■ ACKNOWLEDGMENTS

■ REFERENCES

(1) Knauth, P. Inorganic Solid Li Ion Conductors: An Overview. Solid State Ionics 2009, 180, 911−916.
(2) Fergus, J. W. Ceramic and Polymeric Solid Electrolytes for Lithium-ion Batteries. J. Power Sources 2010, 195, 4554−4569.
(3) Inaguma, Y.; Liquan, C.; Itoh, M.; Nakamura, T.; Uchida, T.; Ikuta, H.; Wakihara, M. High Ionic Conductivity in Lithium Lanthanum Titanate. Solid State Commun. 1993, 86, 689−693.
(4) Inaguma, Y.; Chen, L.; Itoh, M.; Nakamura, T. Candidate Compounds with Perovskite Structure for High Lithium Ionic Conductivity. Solid State Ionics 1994, 70/71, 196−202.
(5) Adachi, G. Y.; Imanaka, N.; Aono, H. Fast Li^+ Conducting Ceramic Electrolytes. Adv. Mater. 1996, 8, 127−135.
(6) Aono, H.; Sugimoto, E.; Sadaoka, Y.; Imanaka, N.; Adachi, G. Y. Ionic Conductivity of the Lithium Titanium Phosphate ($Li_{1+X}M_XTi_{2-X}(PO_4)_3$, M = Al, Sc, Y, and La) Systems. J. Electrochem. Soc. 1989, 136, 590−591.
(7) Arbi, K.; Rojo, J. M.; Sanz, J. Lithium Mobility in Titanium Based Nasicon $Li_{1+x}Ti_{2-x}Al_x(PO_4)_3$ and $LiTi_{2-x}Zr_x(PO_4)_3$ Materials Fol-

lowed by NMR and Impedance Spectroscopy. J. Eur. Ceram., Soc. 2007, 27, 4215−4218.
(8) Aono, H.; Sugimoto, E.; Sadaoka, Y.; Imanaka, N.; Adachi, G. Y. Electrical Property and Sinterability of $LiTi_2(PO_4)_3$ Mixed With Lithium Salt (Li_3PO_4 or Li_3BO_3). Solid State Ionics 1991, 47, 257−264.
(9) Hong, H. Y. P. Crystal Structures and Ionic Conductivity of $Li_{14}Zn(GeO_4)_4$ and other New Li^+ Superionic Condutors. Mater. Res. Bull. 1978, 13, 117−124.
(10) Murayama, M.; Kanno, R.; Irie, M.; Ito, S.; Hata, T.; Sonoyama, N.; Kawamoto, Y. Synthesis of New Lithium Ionic Conductor Thio-LISICON-Lithium Silicon Sulfides System. J. Solid State Chem. 2002, 168, 140−148.
(11) Thangadurai, V.; Kaack, H.; Weppner, W. Novel Fast Lithium Ion Conduction in Garnet-Type $Li_5La_3M_2O_{12}$(M =Nb, Ta). J. Am. Ceram. Soc. 2003, 86, 437−440.
(12) Thangadurai, V.; Weppner, W. $Li_6ALa_2Ta_2O_{12}$ (A = Sr, Ba): Novel Garnet-Like Oxides for Fast Lithium Ion Conduction. Adv. Funct. Mater. 2005, 15, 107−112.
(13) Murugan, R.; Thangadurai, V.; Weppner, W. Fast Lithium Ion Conduction in Garnet-Type $Li_7La_3Zr_2O_{12}$. Angew. Chem., Int. Ed. 2007, 46, 7778−7781.
(14) Thangadurai, V.; Weppner, W. $Li_6ALa_2Nb_2O_{12}$ (A=Ca, Sr, Ba): A New Class of Fast Lithium Ion Conductors with Garnet-Like Structure. J. Am. Ceram. Soc. 2005, 88, 411−418.
(15) Murugan, R.; Weppner, W.; Schmid-Beurmann, P.; Thangadurai, V. Structure and Lithium Ion Conductivity of Garnet-Like $Li_5La_3Sb_2O_{12}$ and $Li_6SrLa_2Sb_2O_{12}$. Mater. Res. Bull. 2008, 43, 2579−2591.
(16) Thangadurai, V.; Weppner, W. Effect of Sintering on the Ionic Conductivity of Garnet-Related Structure $Li_5La_3Nb_2O_{12}$ and In- and K-Doped $Li_5La_3Nb_2O_{12}$. J. Solid State Chem. 2006, 179, 974−984.
(17) Murugan, R.; Weppner, W.; Schmid-Beurmann, P.; Thangadurai, V. Structure and Lithium Ion Conductivity of Bismuth Containing Lithium Garnets $Li_5La_3Bi_2O_{12}$ and $Li_6SrLa_2Bi_2O_{12}$. Mater. Sci. Eng., B 2007, 143, 14−20.
(18) Murugan, R.; Thangadurai, V.; Weppner, W. Lithium Ion Conductivity of $Li_{5+x}Ba_xLa_{3-x}Ta_2O_{12}$ ($x = 0−2$) with Garnet-Related Structure in Dependence of the Barium Content. Ionics 2007, 13, 195−203.
(19) Murugan, R.; Thangadurai, V.; Weppner, W. Effect of Lithium Ion Content on the Lithium Ion Conductivity of the Garnet-Like Structure $Li_{5+x}BaLa_2Ta_2O_{11.5+0.5x}$ ($x = 0−2$). Appl. Phys. A: Mater. Sci. Process. 2008, 91, 615−620.
(20) Zaib, T.; Ortner, M.; Murugan, R.; Weppner, W. Fast Ionic Conduction in Cubic Hafnium Garnet $Li_7La_3Hf_2O_{12}$. Ionics 2010, 16, 855−858.
(21) Kumazaki, S.; Iriyama, Y.; Kim, K. H.; Murugan, R.; Tanabe, K.; Yamamoto, K.; Hirayama, T.; Ogumi, Z. High Lithium Ion Conductive $Li_7La_3Zr_2O_{12}$ by Inclusion of Both Al and Si. Electrochem. Commun. 2011, 13, 509−512.
(22) Awaka, J.; Kijima, N.; Hayakawa, H.; Akimoto, J. Synthesis and Structure Analysis of Tetragonal $Li_7La_3Zr_2O_{12}$ with the Garnet-Related Type Structure. J. Solid State Chem. 2009, 182, 2046−2052.
(23) Awaka, J.; Takashima, A.; Kataoka, K.; Kijima, N.; Idemoto, Y.; Akimoto, J. Crystal Structure of Fast Lithium-Ion-Conducting Cubic $Li_7La_3Zr_2O_{12}$. Chem. Lett. 2011, 40, 60−62.
(24) Geiger, C. A.; Alekseev, E.; Lazic, B.; Fisch, M.; Armbruster, T.; Langner, R.; Fechtelkord, M.; Kim, N.; Pettke, T.; Weppner, W. Crystal Chemistry and Stability of "$Li_7La_3Zr_2O_{12}$" Garnet: A Fast Lithium-Ion Conductor. Inorg. Chem. 2011, 50, 1089−1097.
(25) Kotobuki, M.; Kanamura, K.; Sato, Y.; Yoshida, T. Fabrication of All-Solid-State Lithium Battery With Lithium Metal Anode Using Al_2O_3-Added $Li_7La_3Zr_2O_{12}$ Solid Electrolyte. J. Power Sources 2011, 196, 7750−7754.
(26) Duevel, A.; Kuhn, A.; Robben, L.; Wilkening, M.; Heitjans, P. Mechanosynthesis of Solid Electrolytes: Preparation, Characterization, and Li Ion Transport Properties of Garnet-Type Al-Doped $Li_7La_3Zr_2O_{12}$ Crystallizing with Cubic Symmetry. J. Phys. Chem. C 2012, 116, 15192−15202.

(27) Kim, K. H.; Iriyama, Y.; Yamamoto, K.; Kumazaki, S.; Asaka, T.; Tanabe, K.; Fisher, C. A. J.; Hirayama, T.; Murugan, R.; Ogumi, Z. Characterization of the Interface Between $LiCoO_2$ and $Li_7La_3Zr_2O_{12}$ in an All-Solid-State Rechargeable Lithium Battery. *J. Power Sources* **2011**, *196*, 764−767.

(28) Rangasamy, E.; Wolfenstine, J.; Sakamoto, J. The Role of Al and Li Concentration on the Formation of Cubic Garnet Solid Electrolyte of Nominal Composition $Li_7La_3Zr_2O_{12}$. *Solid State Ionics* **2012**, *206*, 28−32.

(29) Ohta, S.; Kobayashi, T.; Asaoka, T. High Lithium ionic Conductivity in the Garnet-type Oxide $Li_{7-X} La_3(Zr_{2-X}, Nb_X)O_{12}$ (X = 0−2). *J. Power Sources* **2011**, *196*, 3342−3345.

(30) Janani, N.; Ramakumar, S.; Murugan, R. Fast lithium ion conduction in zirconium containing garnet structured ceramic electrolyte, *3rd International Congress on Ceramics (ICC3)*, Osaka, Japan, 2010; pp S9A−P017.

(31) Wang, Y.; Lai, W. High Ionic Conductivity Lithium Garnet Oxides of $Li_{7-x}La_3Zr_{2-x}Ta_xO_{12}$ Compositions. *Electrochem. Solid-State Lett.* **2012**, *15*, A68−A71.

(32) Li, Y.; Wang, C. A.; Xie, H.; Cheng, J.; Goodenough, J. B. High Lithium Ion Conduction in Garnet-type $Li_6La_3ZrTaO_{12}$. *Electrochem. Commun.* **2011**, *13*, 1289−1292.

(33) Buschmann, H.; Berendts, S.; Mogwitz, B.; Janek, J. Lithium Metal Electrode Kinetics and Ionic Conductivity of the Solid Lithium Ion Conductors "$Li_7La_3Zr_2O_{12}$" and $Li_{7-x}La_3Zr_{2-x}Ta_xO_{12}$ with Garnet-type Structure. *J. Power Sources* **2012**, *206*, 236−244.

(34) Logeat, A.; Koehler, T.; Eisele, U.; Stiaszny, B.; Harzer, A.; Tovar, M.; Senyshyn, A.; Ehrenberg, H.; Kozinsky, B. From Order to Disorder: The Structure of Lithium-Conducting Garnets $Li_{7-x}La_3Ta_xZr_{2-x}O_{12}$ (x=0−2). *Solid State Ionics* **2012**, *206*, 33−38.

(35) Li, Y.; Han, J.; Wang, C. A.; Xie, H.; Goodenough, J. B. Optimizing Li^+ Conductivity in a Garnet Framework. *J. Mater. Chem.* **2012**, *22*, 15357−15361.

(36) Murugan, R.; Ramakumar, S.; Janani, N. High Conductive Yttrium Doped $Li_7La_3Zr_2O_{12}$ Cubic Lithium Garnet. *Electrochem. Commun.* **2011**, *13*, 1373−1375.

(37) Dumon, A.; Huang, M.; Shen, Y.; Nan, C. W. High Li ion Conductivity in Strontium Doped $Li_7La_3Zr_2O_{12}$ Garnet. *Solid State Ionics* **2013**, *243*, 36−41.

(38) Ramakumar, S.; Satyanarayana, L.; Manorama, S. V.; Murugan, R. Structure and Li^+ Dynamics of Sb-doped $Li_7La_3Zr_2O_{12}$ Fast Lithium Ion Conductors. *Phys. Chem. Chem. Phys.* **2013**, *15*, 11327−11338.

(39) Deviannapoorani, C.; Dhivya, L.; Ramakumar, S.; Murugan, R. Lithium Ion Transport Properties of High Conductive Tellurium Substituted $Li_7La_3Zr_2O_{12}$ Cubic Lithium Garnets. *J. Power Sources* **2013**, *240*, 18−25.

(40) Rangasamy, E.; Wolfenstine, J.; Allen, J.; Sakamoto, J. The Effect of 24c-site (A) Cation Substitution on the Tetragonal-Cubic Phase Transition in $Li_{7-x}La_{3-x}A_xZr_2O_{12}$ Garnet-Based Ceramic Electrolyte. *J. Power Sources* **2013**, *230*, 261−266.

(41) Huang, M.; Dumon, A.; Nan, C. W. Effect of Si, In and Ge Doping on High Ionic Conductivity of $Li_7La_3Zr_2O_{12}$. *Electrochem. Commun.* **2012**, *21*, 62−64.

(42) Dhivya, L.; Janani, N.; Palanivel, B.; Murugan, R. Li^+ transport Properties of W Substituted $Li_7La_3Zr_2O_{12}$ Cubic Lithium Garnets. *AIP Adv.* **2013**, *3*, 082115−21.

(43) Ohta, S.; Kobayashi, T.; Seki, J.; Asaoka, T. Electrochemical Performance of an All-Solid-State Lithium Ion Battery with Garnet-type Oxide Electrolyte. *J. Power Sources* **2012**, *202*, 332−335.

(44) Ishiguro, K.; Nakata, Y.; Matsui, M.; Uechi, I.; Takeda, Y.; Yamamoto, O.; Imanishi, N. Stability of Nb-Doped Cubic $Li_7La_3Zr_2O_{12}$ with Lithium Metal. *J. Electrochem. Soc.* **2013**, *160*, A1690−A1693.

(45) Nakayama, M.; Kotobuki, M.; Munakata, H.; Nogami, M.; Kanamura, K. First-Principles Density Functional Calculation of Electrochemical Stability of Fast Li Ion Conducting Garnet-type Oxides. *Phys. Chem. Chem. Phys.* **2012**, *14*, 10008−10014.

(46) Liu, K.; Ma, J. T.; Wang, C. A. Excess Lithium Salt Functions More Than Compensating for Lithium Loss when Synthesizing $Li_{6.5}La_3Ta_{0.5}Zr_{1.5}O_{12}$ in Alumina Crucible. *J. Power Sources* **2014**, *260*, 109−114.

(47) Yang, C.; Qiu, L. Y.; Xin, G. X. Densification and Lithium Ion Conductivity of Garnet-type $Li_{7-x}La_3Zr_{2-x}Ta_xO_{12}$ (x = 0.25) Solid Electrolytes. *Chin. Phys. B* **2013**, *22*, 078201−5.

(48) Kihira, Y.; Ohta, S.; Imagawa, H.; Asaoka, T. Effect of Simultaneous Substitution of Alkali Earth Metals and Nb in $Li_7La_3Zr_2O_{12}$ on Lithium-Ion Conductivity. *ECS Electrochem. Lett.* **2013**, *2*, A56−A59.

(49) Miara, L. J.; Ong, S. P.; Mo, Y.; Richards, W. D.; Park, Y.; Lee, J. M.; Lee, H. S.; Ceder, G. Effect of Rb and Ta Doping on the Ionic Conductivity and Stability of the Garnet $Li_{7+2x-y}(La_{3-x}Rb_x)(Zr_{2-y}Ta_y)$-$O_{12}$ ($0 \leq x \leq 0.375, 0 \leq y \leq 1$) Superionic Conductor: A First Principles Investigation. *Chem. Mater.* **2013**, *25*, 3048−3055.

(50) Shannon, R. D. Revised Effective Ionic Radii and Systematic Studies of Interatomic Distances in Halides and Chalcogenides. *Acta Crystallogr., Sect. A: Cryst. Phys., Diffr., Theor. Gen. Crystallogr.* **1976**, *32*, 751−767.

(51) Larraz, G.; Orera, A.; Sanjuan, M. L. Cubic Phases of Garnet-Type $Li_7La_3Zr_2O_{12}$: the Role of Hydration. *J. Mater. Chem. A* **2013**, *1*, 11419−11428.

(52) Chen, Y. S.; Fierro, J. L. G.; Tanaka, T.; Wachs, I. E. Supported Tantalum Oxide Catalysts: Synthesis, Physical Characterization, and Methanol Oxidation Chemical Probe Reaction. *J. Phys. Chem. B* **2003**, *107*, 5243−5250.

(53) Julien, C. 4-V Cathode Materials for Rechargeable Lithium Batteries Wet-Chemistry Synthesis, Structure and Electrochemistry. *Ionics* **2000**, *6*, 30−46.

(54) Julien, C. M.; Massot, M. Lattice Vibrations of Materials for Lithium Rechargeable Batteries. *Mater. Sci. Eng., B* **2003**, *100*, 69−78.

(55) Tietz, F.; Wegener, T.; Gerhards, M. T.; Giarola, M.; Mariotto, G. Synthesis and Raman Micro-spectroscopy Investigation of $Li_7La_3Zr_2O_{12}$. *Solid State Ionics* **2013**, *230*, 77−82.

(56) Wang, X. P.; Xia, Y.; Hu, J.; Xia, Y. P.; Zhuang, Z.; Guo, I. J.; Lu, H.; Zhang, T.; Fang, Q. F. Phase Transition and Conductivity Improvement of Tetragonal Fast Lithium Ionic Electrolyte $Li_7La_3Zr_2O_{12}$. *Solid State Ionics* **2013**, *253*, 137−142.

(57) Wang, W.; Wang, X. P.; Gao, Y. X.; Yang, J. F.; Fang, Q.-F. Investigation on the Stability of $Li_5La_3Ta_2O_{12}$ Lithium Ionic Conductors in Humid Environment. *Front. Mater. Sci. China* **2010**, *4*, 189−192.

(58) Galven, C.; Dittmer, J.; Suard, E.; Le Berre, F.; Crosnier-Lopez, M. P. Instability of Lithium Garnets Against Moisture. Structural Characterization and Dynamics of $Li_{7-x}H_xLa_3Sn_2O_{12}$ and $Li_{5-x}H_xLa_3Nb_2O_{12}$. *Chem. Mater.* **2012**, *24*, 3335−3345.

(59) Buschmann, H.; Dolle, J.; Berendts, S.; Kuhn, A.; Bottke, P.; Wilkening, M.; Heitjans, P.; Senyshyn, A.; Ehrenberg, H.; Lotnyk, A.; Duppel, V.; Kienle, L.; Janek, J. Structure and Dynamics of the Fast Lithium Ion Conductor "$Li_7La_3Zr_2O_{12}$. *Phys. Chem. Chem. Phys.* **2011**, *13*, 19378−19392.

(60) Thompson, T.; Wolfenstine, J.; Allen, J. L.; Johannes, M.; Huq, A.; David, I. N.; Jeff Sakamoto, J. Tetragonal vs. Cubic Phase Stability in Al − free Ta Doped $Li_7La_3Zr_2O_{12}$ (LLZO). *J. Mater. Chem. A* **2014**, *2*, 13431−13436.